Multichannel quantum defect analysis of the double resonance photoionization series of H_2O

M. S. Child[a)]
Physical and Theoretical Chemistry Laboratory, South Parks Road, Oxford OX1 1QZ, United Kingdom

W. L. Glab
Department of Physics, Texas Tech. University, P.O. Box 41051, Lubbock, Texas 79409

(Received 22 September 1999; accepted 1 December 1999)

A new analysis is presented of the recent photoionization spectrum of H_2O, excited by double resonance via several rotational sublevels of the (100) vibrational level of the $\tilde{C}(^1B_1)$ state. Evidence for a previously unsuspected strong *f* series indicates significant *d* orbital contamination of the nominal *p* orbital in the intermediate state. This is the first report of an *f* series in the Rydberg state of any asymmetric top. Previous *d* series analyses of single-photon photoionization spectra terminating on the (100) level of H_2O^+ are also corrected and extended to a wider range of excited rotational electronic states. The *d* series appears to contain absent lines, indicative of predissociation. Some lines remain unassigned, but there is no systematic evidence of either *s* or *p* series. © *2000 American Institute of Physics.* [S0021-9606(00)01408-2]

I. INTRODUCTION

The Rydberg spectrum of H_2O is the best studied of any polyatomic molecule, and also among the most challenging, if only because the entire electronically excited spectrum can be regarded as Rydberg-like at geometries close to the ground-state minimum. All states in the first Rydberg system arise in pairs according to whether the Rydberg electron is attached to the lowest bent $\tilde{X}(^2B_1)$ or lowest linear $\tilde{A}(^2A_1)$ state of H_2O^+. The first two $3s\tilde{A}(^1B_1)$ and $3s\tilde{B}(^1A_1)$ states are dissociative and details of their photodissociation dynamics, to produce H+OH, have attracted considerable attention,[1,2] but there is also a known $4s\tilde{D}'(^1B_1)$ state[3] with discrete rotational structure. Of the three bent $3p$ states, only the $\tilde{C}(^1B_1)$[4–6] state and its $4p$ analog[7] are rotationally resolvable; the $\tilde{D}(^1A_1)$ state[8] is predissociated by configuration interaction[9,10] with $\tilde{B}(^1A_1)$ and the third $^1A_2$ state is thought to dissociate directly to $O(^1D)+H_2$.[11] The five Coriolis coupled $3d$ bent-state absorption bands have also been rotationally analyzed.[3,12] There is also a known bending progression of the linear $3p(^1B_2)$ state,[13] whose $K'\neq 0$ branches seem to be fully predissociated by Renner–Teller coupling to the missing $3p(^1A_2)$ state. The analyzed bent-state bands also show evidence of rotationally selective predissociation[6,7,12,13] and perturbations[12] presumably due to interaction with the various linear states. At shorter wavelengths, Watanabe and Zelikoff[14] and Ishiguro *et al.*[15] assign the main absorption bands below the first ionization limit to *d* series converging on the (000) and (100) vibrational limits of the bent $\tilde{X}(^2B_1)$ state of H_2O^+, with weaker *p* series interpolating between them up to $n=8$. Finally, further rotationally resolved information is available from the jet-cooled photoionization and $1+1$ multiphoton ionization (MPI) spectra,[16,17] which have been assigned[17,18] to the $\tilde{X}\rightarrow nd$ series, with $n=6-11$, terminating on the (000) and (100) vibrational limits. There is, however, no evidence of the interpolating *np* series, perhaps because predissociation, which is known to occur up to and beyond the first ionization limit[19] is too fast compared with the relevant ionization process.

The purpose of this paper is to show that the new double resonance spectra[20,21] contain a wealth of valuable new information. The spectra were excited via selected rotational levels of the $\tilde{C}(^1B_1)(100)$ vibrational state, with Franck–Condon selection for photoionization detection of series converging on the $H_2O^+(100)$ limit. Overlapping series converging on other limits can therefore be discounted. Knowledge of the initial rotational level confirms the strongest line assignments in the earlier jet-cooled single-photon spectra,[16–18] after proper allowance for the change in selection rules between the $\tilde{X}(^1A_1)\rightarrow nd$ and $\tilde{C}(^1B_1)\rightarrow nd$ spectra. Some weaker line assignments are, however, brought into question. The most striking feature is a strong $\tilde{C}(^1B_1)\rightarrow nf$ series, which is the first to be detected for any asymmetric top. Assignment of the *d* series is more difficult, but the overall structure of the $\tilde{C}\rightarrow nd$ spectrum is found to be well reproduced on the basis of five assumed quantum defects, without attempting as yet to include possible effects of linear state perturbations. Some unassigned lines remain, but there is insufficient evidence to identify definitive *s* or *p* series. The intention is to employ the above assignments in a later study of the influence of *l* mixing on the photoelectron branching ratios between different rotational states of H_2O^+.[21] Such *l* mixing was also found to affect the optimized quantum defects, but without perceptibly altering the calculated energies levels. Results are therefore reported below without *l* mixing.

The analysis is based on the multichannel quantum defect formulation for rotational channel interactions in asym-

a)Electronic mail: mark.child@chemistry.ox.ac.uk

metric tops,[18] because interpenetration of clusters with neighboring n values for $n>8$ invalidates the alternative Coriolis coupled top description.[12] An outline of the working equations is given in Sec. II below. Evidence for the newly discovered $\tilde{C}\rightarrow nf$ series is presented in Sec. III, where implications for the nature of the excited orbital in the intermediate $\tilde{C}(^1B_1)$ state is also discussed. Analysis of the strong $\tilde{C}\rightarrow nd$ spectrum is presented in Sec. IV. Finally, the main conclusions are summarized and evaluated in Sec. V.

II. EXPERIMENT

The experiment described here made use of multiphoton excitation and ion detection to examine the spectra of the autoionizing states of water lying between the first, vibrationally unexcited ionization limit (000) and the ionization limit built on the ion core with 1 quantum of symmetric stretch vibrational energy (100). In this section, we will describe the excitation scheme and tunable laser sources, the time-of-flight ion mass spectrometer and vacuum system, and data acquisition. This system has been briefly described previously.[20]

Rydberg states of water just above the first ionization limit (101 766 cm^{-1} above the ground state) were excited through stepwise-resonant two-photon excitation, using intermediate resonance with selected rotational levels of the vibronic state. This approach has several important advantages over direct excitation from the ground state. First, the use of intermediate resonance with the rotationally resolved $\tilde{C}(100)$ levels leads to excitation of the Rydberg states from a single well-defined angular momentum state, resulting in drastic simplification of the Rydberg spectrum through the angular momentum selection rules. Also, since the $\tilde{C}$ state is a Rydberg state, its potential energy surface is so similar to those of the final Rydberg states that, by the Franck–Condon principle, excitation from the $\tilde{C}$ state tends to occur with no change in the vibrational quantum number. Thus, excitation from the $\tilde{C}(100)$ vibronic state preferentially populates Rydberg states converging to the (100) vibrational state of the ground electronic state of the ion core, again reducing the spectral congestion and aiding in the identification of the Rydberg states. This behavior has been previously described in other triatomic species.[22] Finally, the use of intermediate resonance makes it possible to avoid the use of XUV (extreme UV) light, which is relatively difficult to generate and propagate.

Light at the various wavelengths required to perform this experiment was generated using a set of three home-built, tunable, pulsed dye lasers pumped by the second and third harmonic outputs of a single Nd^{+3}:YAG laser (Continuum NY-61). The YAG laser produced 5 ns duration pulses at the two harmonic wavelengths with a 10 Hz repetition rate. The vacuum ultraviolet light required to pump the $\tilde{C}(100)\leftarrow\tilde{X}(000)$ transition lies at wavelengths near 120 nm. Rapid predissociation of the rotational levels of the $\tilde{C}(100)$ state with rates of $\sim 10^{11}\,s^{-1}$ acted to deplete the excited state population before further excitation to the Rydberg states could occur, so relatively large pulse energies in the vacuum ultraviolet were required to achieve significant double-resonance signals. Therefore, we used two-photon resonant difference frequency generation in krypton gas to produce the vacuum UV light.[23] In this process, tunable light near 202 and 665 nm was focused with a 15 cm focal length lens into a cell containing about 20 Torr of krypton gas. The 202 nm light was tuned to resonance with the $Kr4p^6\rightarrow\rightarrow 4p^5 5p'[1/2]_0$ transition, and photons at the difference energy between this transition energy and the photon energy of the 665 nm light was generated. The input pulse energy of the 202 nm light was about 200 μJ and about 3 mJ of 665 nm light was used. The tunable light used to excite autoionizing states from the excited level of the state was derived from a third tunable dye laser with a bandwidth of $\sim$0.03 cm^{-1}, and were overlapped in space and time with the VUV beam. Pulse energies of several mJ in a beam diameter of $\sim$3 mm were used in the wavelength range between 555 and 470 nm.

The VUV light propagated into the interaction region of a time-of-flight ion mass spectrometer through a magnesium fluoride window, while the laser light which excited the Rydberg states from the $\tilde{C}(100)$ state entered the vacuum chamber containing the time-of-flight through a quartz window, counterpropagating with the VUV light. Water vapor was fed into the interaction region with an effusive source, and pumped out through the orifice through which ions entered the flight tube. The resulting pressure of room temperature water vapor was set to be several times 10^{-5} Torr by adjusting the water vapor flow rate. The flight tube was evacuated using a small turbomolecular pump. A pulsed electric field of several hundred volts per centimeter was applied after the arrival of the laser pulses to drive the laser-produced ions into the flight tube for mass analysis. A standard arrangement of pulse amplifiers, gating electronics, sample-and-hold circuits, and computerized data acquisition was used to record the spectra as the second laser's photon energy was scanned over the region of autoionization. This procedure was repeated for a number of rotational levels of the state: 0_{00}, 1_{01}, 1_{11}, 1_{10}, and 2_{02}. The second step laser photon energy was calibrated to an accuracy of about 0.5 cm^{-1} through the analysis of a simultaneously acquired optogalvanic spectrum of neon and uranium in a hollow cathode discharge lamp.

III. THEORETICAL CONSIDERATIONS

The main features of the multichannel quantum defect theory (MQDT) for rotational channel interactions in asymmetric tops[18] are first recalled. It is assumed for simplicity that the orbital angular momentum l as well as the total angular momentum J are conserved, an approximation that will be relaxed in a future analysis of the photo-electron branching ratios between different H_2O^+ rotational states. Two angular momentum schemes are employed. Hund's case (b) basis functions

$$|\alpha\rangle=|JlK\lambda,p_e p_r\rangle, \tag{1}$$

where p_e and p_r are electronic parity labels, is assumed to

apply within a short-range core around the positive ion, where the local Rydberg electron energy is assumed to follow the Rydberg formula

$$E_{n\alpha}=I-\mathrm{Ry}/(n-\mu_\alpha)^2, \tag{2}$$

in which Ry is the properly mass-adjusted Rydberg constant, μ_α is the quantum defect for the orbital labeled by $|l\lambda p_e\rangle$, and I is the appropriate ionization energy—in the present case, the energy of the (100) vibrational level of H_2O^+. Outside the core, on the other hand, Hund's case (d) applies, with basis functions

$$|i\rangle=\sum\ c_{N^+K^+}|JlN^+K^+,p\rangle, \quad p=p_e+p_r \tag{3}$$

where the coefficients $c_{N^+K^+}$ are determined by diagonalization of the rotational Hamiltonian of the positive ion,

$$\hat{H}_{\mathrm{rot}}=A^+\hat{N}_a^{+2}+B^+\hat{N}_b^{+2}+C^+\hat{N}_c^{+2}. \tag{4}$$

The corresponding rotational energies are denoted E_i^+. Before turning to the MQDT theory, it is useful to note that the more familiar Coriolis coupled top theory[12] would employ a Hamiltonian of the form

$$\hat{H}=\sum\ |\alpha\rangle E_{n\alpha}\langle\alpha|+\hat{H}_{\mathrm{rot}}, \tag{5}$$

but with $\hat{H}_{\mathrm{rot}}$ expressed in terms of the operators $\hat{\mathbf{J}}$ and $\hat{\mathbf{I}}$, namely

$$\hat{H}_{\mathrm{rot}}=A^+(J_a-l_a)^2+B^+(J_b-l_b)^2+C^+(J_c-l_c)^2, \tag{6}$$

in order to facilitate diagonalization in the case (b) basis. The connection with MQDT is, however, best displayed by transforming to the case (d) basis. The relevant matrix elements take the form

$$\hat{H}_{ij}=\sum_\alpha\ \langle i|\alpha\rangle(E_{n\alpha}-I)\langle\alpha|j\rangle+(I+E_i^+)\delta_{ij}. \tag{7}$$

The physical interpretation is that the series converging on different rotational energy thresholds, $I+E_i^+$, of the positive ion, mutually interact via a term dependent on the frame transformation $\langle i|\alpha\rangle$, between case (d) and case (b) bases and on the quantum defects, μ_α, contained in the $E_{n\alpha}$ via Eq. (2). In either formulation, this Coriolis coupled top theory correctly describes the transformation from case (b), when the electronic energy splittings are large compared with the rotational energy differences $E_i^+-E_j^+$, to case (d), when the opposite inequality applies. Interseries coupling is, however, restricted to a given Rydberg cluster, with a fixed principal quantum number n. Mutichannel quantum defect theory removes this latter restriction.

A full account of MQDT theory[24] is beyond the scope of this paper, but the main difference from traditional methods is that it is formulated in terms of channels, each containing a complete series terminating a given vibrational–rotational–electronic state of the positive ion, coupled to a particular Rydberg angular momentum wave, rather than in terms of normalized basis states. MQDT theory then relies on the physical approximation that interchannel couplings are restricted to within a short-range core, outside of which the Rydberg electron is subject to a pure Coulomb field. Moreover, the femtosecond duration of the electron/core encounters justifies a sudden treatment, by which the electron accesses a Born–Oppenheimer, Hund's case (b), angular momentum state $|\alpha\rangle$, acquires a phase shift, $\pi\mu_\alpha$, dependent on the penetrating power of the relevant orbital and then switches, with probability $|\langle i|\alpha\rangle|^2$, to a Hund's case (d) state, $|i\rangle$ on leaving the core. The upshot of these approximations is that the wave function in the external region can be expressed as

$$\Psi\sim\sum_{i,j}\ |i\rangle[\,\delta_{ij}f_j(E,r)+K_{ij}g_j(E,r)\,]Z_j, \tag{8}$$

in which $f_j(E,r)$ and $g_j(E,r)$ are regular and irregular radial Coulomb wave functions in channel j at total energy E, and the elements of the scattering K matrix are given by

$$K_{ij}=\sum_\alpha\ \langle i|\alpha\rangle\tan\pi\mu_\alpha\langle\alpha|j\rangle. \tag{9}$$

The energy dependence of the known asymptotic approximations to $f_j(E,r)$ and $g_j(E,r)$ (Ref. 24) then leads to cancellation of exponentially divergent terms in Eq. (8), provided that

$$[K+\tan\pi\nu(E)]\mathbf{Z}=0, \tag{10}$$

where $\tan\pi\nu(E)$ is a diagonal matrix, with elements determined by

$$\nu_i(E)=\sqrt{\frac{\mathrm{Ry}}{(I+E_i^+-E)}}. \tag{11}$$

A numerical search for the roots of Eq. (10) therefore replaces the normal matrix diagonalization procedure.

Points of contact with Eqs. (1)–(7) include the fact that the roots of Eqs. (10) and (11) in the single-channel case immediately rearrange to Eq. (2), because each cycle of $\tan\pi\nu(E)$ corresponds to a new principal quantum number. Second, the structural similarity between Eqs. (7) and (9) demonstrates that the electronic–rotational Coriolis interactions are carried by the frame transformation $\langle i|\alpha\rangle$ in the MQDT formulation, rather than by the terms in $J_a l_a$ etc. in Eq. (6). Finally, the vector $\mathbf{Z}$ in Eq. (10) is analogous to the case (d) eigenvector of $\hat{H}$, defined by Eq. (7), except that the components of $\mathbf{Z}$ relate to channels at a given energy rather than to individual states. The important difference between Eq. (10) and Eqs. (6) and (7) is that each cycle of the diagonal terms $\tan\pi\nu_i(E)$ gives rise to a new n value, so that the roots of Eq. (10) describe the entire spectrum, up to the ionization limit, rather than being restricted to a single nl cluster. The MQDT equations are also readily extended to obtain autoionization linewidths and photoionization branching ratios, although we shall at present concentrate solely on the

TABLE I. C_{2v} point group symmetries of different orbitals.

Symm	$l=0$	$l=1$	$l=2$	$l=3$
a_1	$s\sigma_+$	$p\pi_-$	$d\sigma_+, d\delta_+$	$f\pi_+, f\phi_+$
a_2			$d\pi_+$	$f\sigma_+, f\delta_+$
b_1		$p\pi_+$	$d\delta_-$	$f\pi_-, f\phi_-$
b_2		$p\sigma_+$	$d\pi_-$	$f\delta_-$

TABLE II. Propensity rules for the series limits excited from different initial orbitals. Entries in the final line give the total electronic symmetry of the relevant state.

$J''_{K''_aK''_c}$	$p\pi_-$	$p\pi_+$	$d\sigma_+$	$d\delta_+$
0_{00}	1_{11}	1_{10}	2_{02}	2_{20}
1_{01}	$1_{10},2_{12}$	$1_{11},2_{11}$	$1_{01},3_{03}$	$2_{21},3_{21}$
1_{11}	$0_{00},2_{02}$	1_{01}	$1_{11},2_{11},3_{13}$	$1_{11},2_{11},3_{13}$
1_{10}	1_{01}	$0_{00},2_{02}$	$1_{10},2_{12},3_{12}$	$1_{10},2_{12},3_{12}$
2_{02}	$1_{11},2_{11},3_{13}$	$1_{10},2_{12},3_{12}$	$0_{00},2_{02},4_{04}$	$2_{20},3_{22},4_{22}$
State sym	$^1B_1$	$^1A_1$	$^1B_1$	$^1B_1$

autoionization resonance energies, by treating all channels as artificially closed. At a practical level, the input for both the Coriolis coupling method and the MQDT calculation comprises a set of quantum defects, μ_α, the relevant ionization energy, I, and the positive ion rotational constants, A^+, B^+, and C^+. Child and Jungen[18] give specific forms for the frame transformation elements $\langle i|\alpha\rangle$ and for the relevant spectroscopic transition amplitudes, both of which are determined by angular momentum algebra.

In conclusion, it is convenient for what follows to review some important symmetry considerations. In the first place, each Rydberg state has a defined total angular momentum, J, and two strict parity labels[25]

$$p = p_e + p_r, \tag{12}$$

and

$$p^* = p + K + \lambda = p + K^+, \tag{13}$$

although there may be many component channels in a given $\{Jpp^*\}$ block. Optical transitions are subject to the general selection rules $\Delta J = 0, \pm 1$, with $0 \leftrightarrow 0$ forbidden, while both Δp and Δp^* must be odd. To the extent that l is a good quantum number, there are also propensity rules[18] for transitions between an initial case (b) state $|l'',\lambda'',p''_e\rangle J''_{K''_aK''_c}$ and a case (d) state close to the series limit $N^+_{K^+_aK^+_c}$. The following restrictions apply:

$$K_c^+ - K_c'' - (p_e'' + \lambda'' + l'') = \text{even}, \tag{14}$$

$$K_a^+ = |K_a'' - \lambda''|, \tag{15}$$

and

$$N^+ = |J'' - l''|. \tag{16}$$

Finally, for ease of reference, Table I gives the C_{2v} point group symmetries of the different Rydberg orbitals

$$|l\lambda_\pm\rangle = [2(1+\delta_{\lambda 0})]^{1/2}(|l\lambda\rangle + (-1)^{p_e}|l-\lambda\rangle), \tag{17}$$

where the upper or lower sign on the left applies for $p_e = 0$ or $p_e = 1$, respectively. Table II lists the case (d) $N^+_{K^+_aK^+_c}$ limits accessible from different case (b) states, according to the propensity rules (15)–(17).

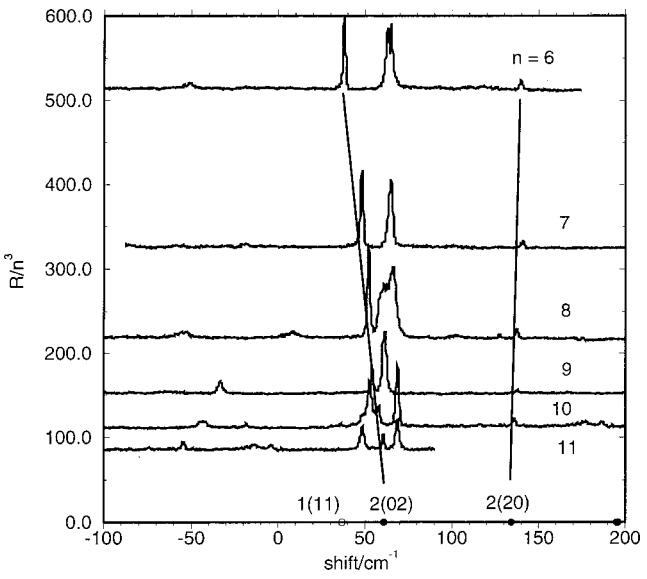

FIG. 1. A scaled presentation of the spectrum excited via the $\tilde{C}(100)0_{00}$ state. Spectra for successive n values are plotted with respect to hydrogenic values by use of Eq. (19). Solid lines indicate nf series terminating on H_2O^+ rotational limits 2_{02} and 2_{20}.

TABLE III. Spectroscopic constants.

	Orbital	μ	Other work (Ref. 17)
Quantum defects	$f\sigma_+$	0.022 79(200)	
	$f\pi_+$	0.014 32(150)	
	$f\pi_-$	0.027 35(230)	
	$f\delta_+$	0.005 88(230)	
	$f\delta_-$	−0.009 348(410)	
	$f\phi_+$	−0.024 514(520)	
	$f\phi_-$	−0.010 454(510)	
	$d\sigma_+$	0.135 63(140)	0.1423
	$d\pi_+$	0.704 07(1180)	0.3196
	$d\pi_-$	0.088 79(350)	0.0704
	$d\delta_+$	−0.007 13(140)	0.0068
	$d\delta_-$	−0.006 75(180)	−0.0008
Vibrational limits		100	010
Ionization energy/cm^{-1}		104 979.0	103 174.4
Rydberg constant/cm^{-1}		109 733.8	109 733.8
Rotational constants			
A^+/cm^{-1}		28.4233	33.3601
B^+/cm^{-1}		12.1795	12.4765
C^+/cm^{-1}		8.2935	8.3188

IV. ASSIGNMENTS TO THE *f* SERIES

The overview, in Fig. 1, of the double resonance spectrum excited from the $\tilde{C}$ (100) 0_{00} intermediate level, gives clear evidence for the presence of an excited f series. Segments for different n values have been combined in a single diagram by plotting the excited state energies on the shifted scale

$$\Delta = \nu_{\text{obs}} - \left(I - \frac{\text{Ry}}{n^2}\right), \tag{18}$$

where ν_{obs} is measured from $\tilde{X}$ (000) 0_{00} and $I = 104\,979\,\text{cm}^{-1}$ is derived from the known first ionization limit (101 766 cm^{-1}) (Ref. 26) and the ν_1 fundamental of H_2O^+ (3213 cm^{-1}).[27] The baselines for successive spectra have been offset by Ry/n^3, so that series fit by the Rydberg-like formula

TABLE IV. *f* series assignments. Energies are measured from the (000) 0_{00} level of the ground electronic state.

$J''_{K''_aK''_c}$	$N^+_{K^+_aK^+_c}$	J'	n	E'_{obs}/cm^{-1}	E'_{calc}/cm^{-1}	$J''_{K''_aK''_c}$	$N^+_{K^+_aK^+_c}$	J'	n	E'_{obs}/cm^{-1}	E'_{calc}/cm^{-1}
0_{00}	2_{02}	1	6	101 968.8	101 969.7				9	103 710.9	103 707.8
			7	102 787.6	102 786.5				10	103 968.9	103 965.6
			8	103 316.1	103 316.0				11	104 160.9	104 156.4
			9	103 678.9	103 678.6						
			10	103 938.6	103 937.8	1_{11}	3_{13}	0	6	102 049.8	102 045.1
			11	104 130.7	104 129.3				7	102 862.6	102 859.1
									8	103 390.9	103 387.0
0_{00}	2_{20}	1	6	102 070.0	102 071.6				9	103 753.1	103 748.7
			7	102 880.8	102 878.8				10	104 011.3	104 007.3
			8	103 401.9	103 402.3						
			9	103 761.8	103 762.2	1_{11}	3_{13}	2	6	102 053.2	102 053.9
			10	104 017.2	104 107.9				7	102 862.6	102 864.3
									8	103 393.6	103 390.3
1_{01}	1_{01}	2	6	101 932.4	101 935.0				9	103 753.1	103 751.0
			7	102 748.3	102 750.0				10	104 011.3	104 008.6
			8	103 277.7	103 278.3						
			9	103 640.6	103 640.0	1_{10}	1_{10}	2	7	102 777.4	102 777.0
			10	103 900.0	103 898.9		2_{12}	2	7	102 809.2	102 810.8
							3_{12}	2	7	102 883.4	102 884.9
1_{01}	3_{03}	1	6	102 029.6	102 030.9	2_{02}	0_{00}	3	6	101 920.0	101 923.0
			7	102 846.6	102 847.0				7	102 733.6	102 735.5
			8	103 375.5	103 376.0				8	103 261.8	103 262.6
			9	103 738.5	103 738.3				9	103 624.5	103 622.8
			10	103 997.6	103 997.2						
						2_{02}	2_{02}	2	6	101 983.0	101 986.3
1_{01}	2_{21}	1	7	102 879.7	102 881.3				7	102 793.5	102 797.2
			8	103 402.6	103 403.7				8	103 322.2	103 322.7
			10	103 403.7	103 403.7						
						2_{02}	2_{02}	3	6	101 995.0	101 995.8
1_{01}	2_{21}	2	6	102 058.4	102 059.8				7	102 801.0	102 802.1
			7	102 870.0	102 870.0				8	103 327.6	103 326.2
			8	103 397.5	103 396.7				9	103 688.0	103 685.6
			9	103 758.8	103 757.6						
			10	104 016.7	104 014.9	2_{02}	2_{20}	3	6	102 049.3	102 050.2
									7	102 863.8	102 864.8
1_{01}	3_{21}	1	6	102 120.8	102 124.1				8	103 394.1	103 392.8
			7	102 933.2	102 934.7				9	103 748.3	103 751.0
			8	103 461.3	103 460.6						
			9	103 820.1	103 821.1	2_{02}	3_{22}	1	6	102 103.5	102 106.6
									7	102 919.9	102 922.7
1_{11}	1_{11}	2	6	101 967.2	101 965.6				8	103 452.2	103 451.7
			7	102 777.5	102 776.3						
			8	103 305.9	103 301.6	2_{02}	3_{22}	2	6	102 110.3	102 112.2
			9	103 659.5	103 661.5				7	102 923.9	102 925.5
			10	103 922.5	103 918.8				8	103 453.8	103 453.3
			11	104 113.9	104 109.2						
						2_{02}	4_{04}	2	6	102 125.7	102 125.1
1_{11}	2_{11}	2	6	102 013.0	102 011.0				7	102 932.2	102 933.8
			7	102 824.4	102 821.3				8	103 458.6	103 458.9
			8	103 347.9	103 347.2						

$$\nu_{obs} = I' - \frac{Ry}{(n-\mu_{eff})^2} \tag{19}$$

will appear as straight lines with slope $(-2\mu_{eff})^{-1}$ and intercept $I'-I$, for sufficiently small (μ_{eff}/n). The quantity μ_{eff} will typically be some case (d) average of the μ_α in Eq. (2).

Evidence for the presence of *f* series comes first from the linearity of the two marked series in Fig. 1, with small quantum defects of 0.0235 and −0.0049, respectively. More importantly, the two intercepts coincide with the filled circles determined by the known[28] 2_{02} and 2_{20} rotational energies of H_2O^+, which are accessible by Eqs. (15)–(17) and the contents of Table II, only by excitation from an even *l* component of the nominal $3p\tilde{C}(^1B_1)$ state. The implication is therefore that the linear series have odd *l* character, while the smallness of the effective quantum defects points to an *f* series, which in turn suggests *d* orbital contamination of the excited $\tilde{C}$ state orbital. Notice that the remaining strong lines in Fig. 1, which are assigned to the $3p\pi_- \rightarrow nd$ series, show no evidence of linear series terminating on the open circle, corresponding to the 1_{11} limit, suggested by Table II, because the spread of *d* orbital quantum defects is too large to allow a near case (d) description at $n=11$.

Confirmation of the proposed *f* series assignment is provided by the detailed spectroscopic fit listed in Tables III and IV. The seven quantum defects in Table III were optimized to 68 upper-state energies derived from linear series analogous to those marked in Fig. 1, for the double resonance

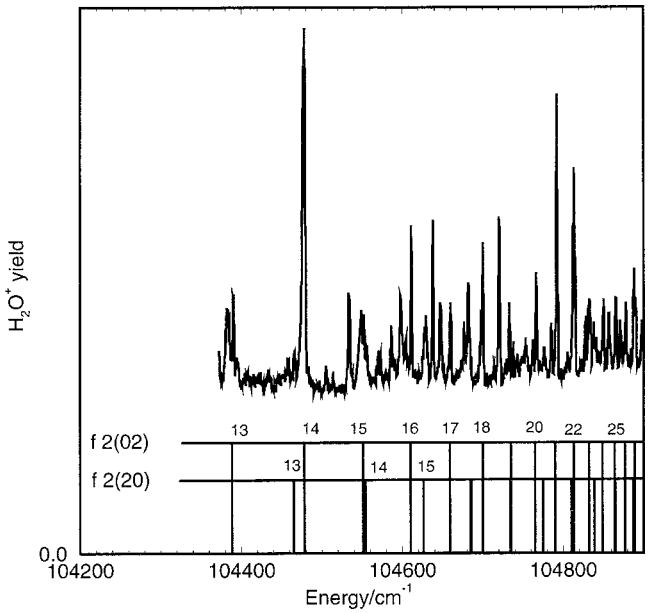

FIG. 2. Extrapolation of the $\tilde{C}(100)0_{00}\rightarrow nf$ spectrum.

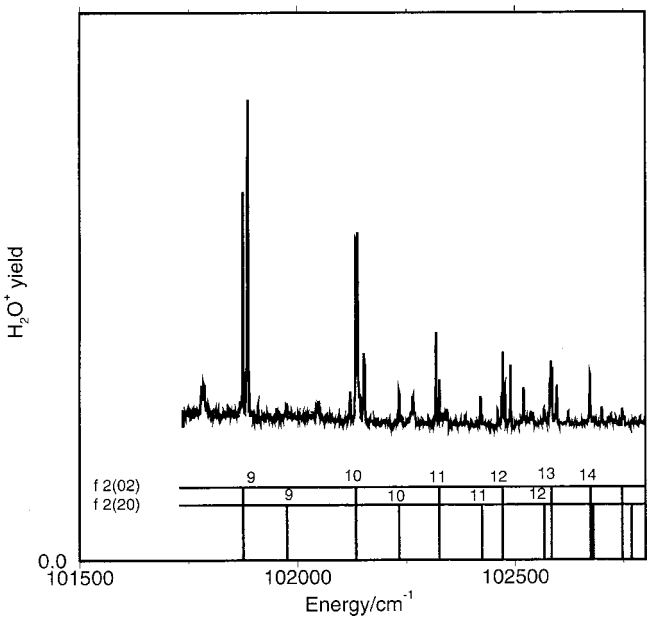

FIG. 3. Extrapolation of the $\tilde{C}(010)0_{00}\rightarrow nf$ spectrum.

spectra involving intermediate 0_{00}, 1_{01}, 1_{11}, and 2_{02} rotational levels of the $3p\tilde{C}(^1B_1)(100)$ state. The resulting rms deviation is 2.37 cm^{-1} and a comparison between observed and calculated upper-state energy levels is given in Table IV.

As further evidence, Figs. 2 and 3 show extrapolations to higher n values of the spectra excited from $\tilde{C}(100)0_{00}$ and $\tilde{C}(010)0_{00}$. The quantum defects in Table III were employed in both cases, but the rotational constants and ionization limits were adjusted according to the relevant vibrational state.

V. ASSIGNMENTS TO THE *d* SERIES

Analysis of the $\tilde{C}\rightarrow nd$ spectrum proves more difficult than that of the earlier jet-cooled $X\rightarrow nd$ photoionization spectra,[16,17] or indeed of the above $\tilde{C}\rightarrow nf$ spectrum, despite having knowledge of the intermediate $\tilde{C}(100)$ rotational level. Complexity with respect to the earlier spectra comes from the fact that jet-cooling populated only the lowest *para* 0_{00} and *ortho* 1_{01} rotational levels, so that the strongest lines were all excited from $\tilde{X}(000)1_{01}$ to the symmetry blocks $\{J'pp^*\}=\{101\}$ or $\{201\}$, whereas the double resonance spectra include transitions from $\tilde{C}(100)0_{00}$, 1_{01}, 1_{11}, and 2_{02}. Consequently there are many more lines to be accounted for. Moreover, the spread of *d* orbital quantum defects obtained in previous studies,[16,17] from 0 to 0.32, precludes the existence of linear series such as those in Fig. 1, except in special cases (see below). Finally, there are also possible complications due to predissociation and/or perturbations, due to interactions with *nl* series associated with the linear $\tilde{A}(^2A_1)$ state of H_2O^+.

The complexities involved in the analysis may be understood by examining the list of contributing channels in the relevant symmetry blocks $\{J'pp^*\}$ given in Table V; relevant intermediate rotational levels are also indicated in the final row, so that, for example transitions from $\tilde{C}\ 1_{11}$ go to $\{J'00\}$ with $J'=0$, 1, and 2, while those from $\tilde{C}\ 0_{00}$ go to $\{101\}$. One immediate observation is that the blocks $\{001\}$, $\{010\}$, and $\{011\}$ each involve only a single channel, which means in principle that transitions to these blocks should give rise to ''linear series'' in the sense of Fig. 1, from which the $d\pi_-$, $d\pi_+$, and $d\delta_-$ quantum defects could be immediately deduced, because there are no possible interchannel interactions to disturb the linearity of the plots. Unfortunately, however, transitions to the $\{001\}$ block are symmetry forbidden from the $\tilde{C}$ state, those for $\tilde{C}\ 1_{01}\rightarrow\{010\}$ lie outside the range of the observed spectra for $n=6$ and 7, while spectra from $\tilde{C}\ 1_{10}\rightarrow\{J'11\}$ are available only for $n=7$. It should also be added that the change of electronic selection

TABLE V. Case (b) channels contibuting to different symmetry blocks $\{J'pp^*\}$. The bottom row indicates the intermediate rotational level relevant to excitation to the given block, subject to normal selection rules on *J*.

J'	$l\lambda_\pm$	$\{J'00\}$	$\{J'01\}$	$\{J'10\}$	$\{J'11\}$
0	$d\sigma_+$	0_{00}			
	$d\pi_+$			0_{00}	
	$d\pi_-$		0_{00}		
	$d\delta_+$	0_{00}			
	$d\delta_-$				0_{00}
1	$d\sigma_+$		1_{11}	1_{10}	1_{01}
	$d\pi_+$	1_{10}	1_{01}		1_{11}
	$d\pi_-$	1_{11}		1_{01}	1_{10}
	$d\pi_+$		1_{11}	1_{10}	1_{01}
	$d\delta_-$	1_{01}	1_{10}	1_{11}	
2	$d\sigma_+$	$2_{02},2_{20}$	2_{11}	2_{12}	2_{21}
	$d\pi_+$	2_{12}	2_{21}	$2_{02},2_{20}$	2_{11}
	$d\pi_-$	2_{11}	$2_{02},2_{20}$	2_{21}	2_{12}
	$d\delta_+$	$2_{02},2_{20}$	2_{11}	2_{12}	2_{21}
	$d\delta_-$	2_{21}	2_{12}	2_{11}	$2_{02},2_{20}$
$J''_{K''_aK''_c}$		1_{11}	$0_{00},2_{02}$	1_{01}	1_{10}

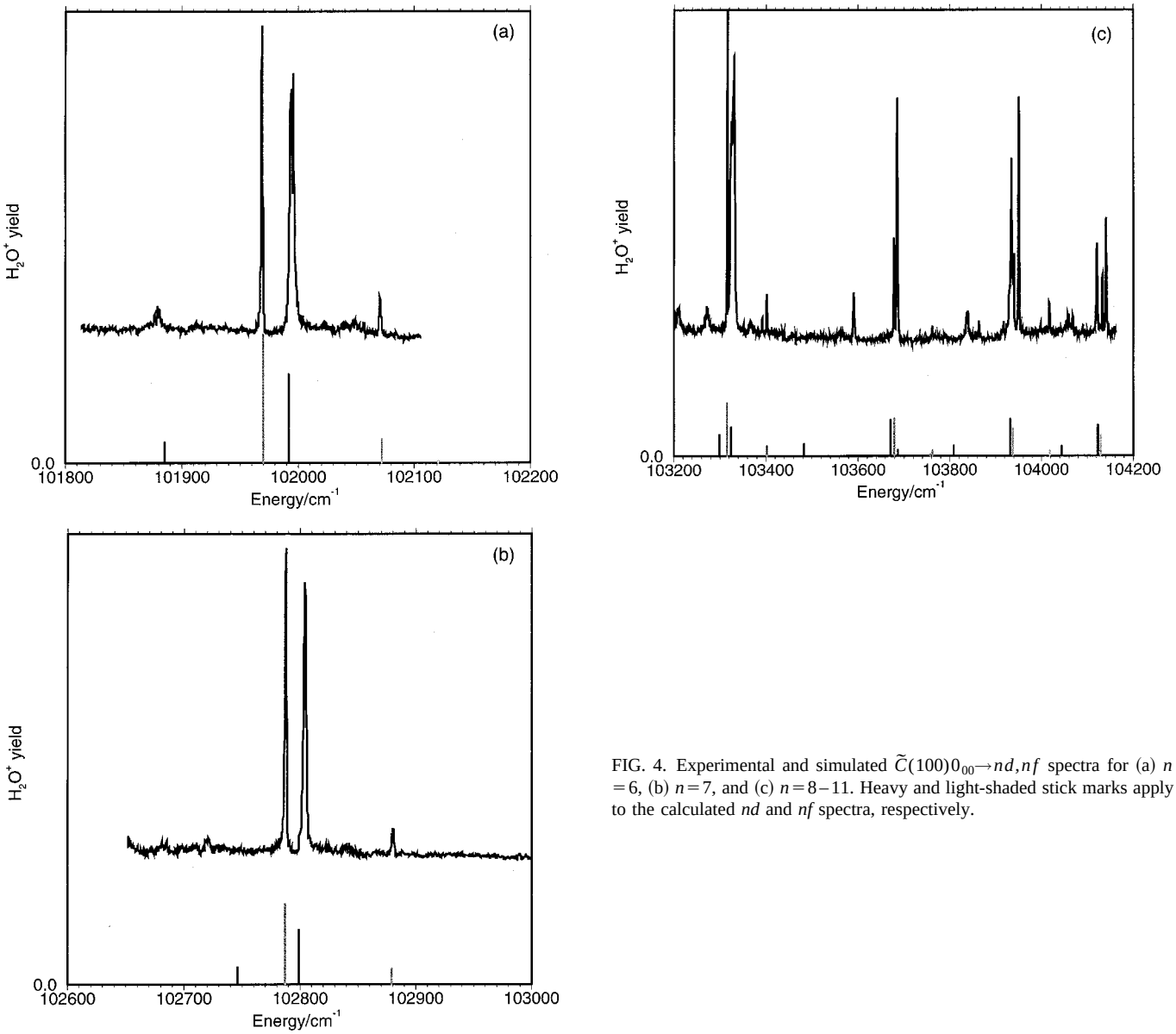

FIG. 4. Experimental and simulated $\tilde{C}(100)0_{00}\rightarrow nd,nf$ spectra for (a) $n=6$, (b) $n=7$, and (c) $n=8-11$. Heavy and light-shaded stick marks apply to the calculated *nd* and *nf* spectra, respectively.

rules should in principle give rise to a linear $\tilde{X}\ 1_{01}\rightarrow\{001\}$ series in the single-photon photoionization spectra of Page *et al.*[16] and Vrakking *et al.*;[17] but no such series can be detected, presumably due to perturbations by a linear state of $^1B_2$ symmetry, as discussed by Child.[7] Direct determination of the defects $\mu(d\pi_-)$, $\mu(d\pi_+)$, and $\mu(d\delta_-)$ is therefore precluded. Fortunately, however, plausible linear series in the $\tilde{C}1_{11}\rightarrow nd$ spectrum, whose *P* branch lines go to the {000} symmetry block, can be employed to determine $\mu(d\sigma_+)$ and $\mu(d\delta_+)$.

The remaining quantum defects must be determined more indirectly. The most helpful observation is that previous analyses[12,17,18] have established that $\mu(d\delta_-),\mu(d\delta_+)$ are extremely close—to the extent for example that Gilbert *et al.*[12] find that the two components of the $3d(000)\,\tilde{F}(^1A_1,^1B_1)$ are separated by only 16 cm^{-1}. Consequently, essentially complete Coriolis mixing between levels with $K'\neq 0$ leads to intensity pooling and cancellation. An important particular example occurs in the {101} symmetry block (see Table V), which is accessible from $\tilde{C}\ 0_{00}$. Most of the strong unassigned lines in Fig. 1 in fact belong to the coupled states

$$|na\rangle=\frac{1}{\sqrt{2}}(|nd\delta_+1_{11}\rangle+|nd\delta_-1_{10}\rangle, \tag{20}$$

whose energies [combined with knowledge of $\mu(d\delta_+)$] serve to determine $\mu(d\delta_-)$. Further information comes from similar coupling in the {110} block, which is accessible from $\tilde{C}\ 1_{01}$. To the extent that other interactions are ignored, one predicts the existence of an analogous state

$$|na'\rangle=\frac{1}{\sqrt{2}}(|nd\delta_+1_{10}\rangle+|nd\delta_-1_{11}\rangle, \tag{21}$$

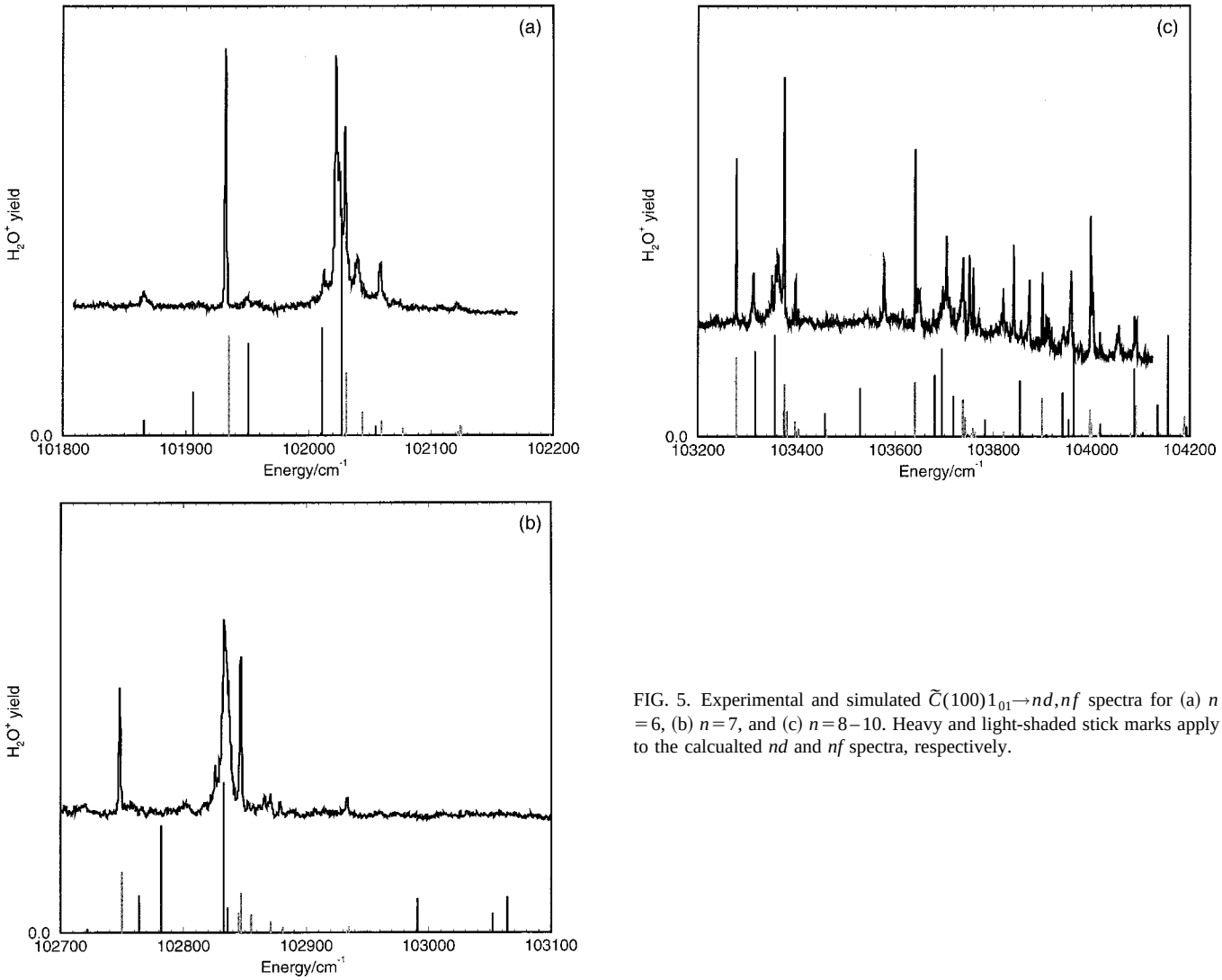

FIG. 5. Experimental and simulated $\tilde{C}(100)1_{01}\rightarrow nd,nf$ spectra for (a) $n=6$, (b) $n=7$, and (c) $n=8-10$. Heavy and light-shaded stick marks apply to the calcualted *nd* and *nf* spectra, respectively.

which is predicted to be degenerate with $|na\rangle$. Yet the $\tilde{C}\ 1_{01}$ spectrum for $n=6$ is found to contain no state with an energy close to that implied by the $|6a\rangle$ line in the $\tilde{C}\ 0_{00}$ spectrum at 101 995 cm^{-1}. Comparison between the compositions of the {101} and {110} symmetry blocks in Table V shows that the difference must be attributable to Coriolis interactions with either the $d\pi_+\ 1_{01}$ channel in {101} or the $d\pi_-\ 1_{01}$ channel in {110}, of which the latter is more likely in view of the smaller $d\pi_-$ quantum defect obtained in earlier studies.[12,17,18] A more precise value of this latter defect was therefore deduced by assigning lines in the $\tilde{C}\ 1_{01}\rightarrow 6d$ spectrum at 101 949.9 cm^{-1} and 102 016.0 cm^{-1} to the upper and lower levels arising from this perturbation in the {110} symmetry block. Finally, given provisional values for the four quantum defects $\mu(d\sigma_+)$, $\mu(d\pi_-)$, $\mu(d\delta_+)$, and $\mu(d\delta_-)$, the fifth defect, $\mu(d\pi_+)$, was determined by least-squares optimization to a very strong line in the {301} branch of the $\tilde{C}\ 2_{02}$ spectrum, which was one of the few strong lines otherwise not well reproduced by the MQDT fit for $n=6-8$. Refinements to the resulting quantum defects were obtained by least-squares optimization to (i) the two linear series assigned to $\tilde{C}\ 1_{11}\rightarrow\{000\}$ transitions, (ii) the strong lines in the $\tilde{C}\ 0_{00}\rightarrow\{101\}$ spectrum, and (iii) the specific $\tilde{C}\ 1_{01}\rightarrow\{110\}$ and $\tilde{C}\ 2_{02}\rightarrow\{301\}$ transitions mentioned above. A total of 19 lines were included in the fit, with an rms deviation of 2.74 cm^{-1}. The resulting quantum defects are listed in Table III. It is evident that four of the values are in good agreement with those of Vrakking *et al.*[17] but that $\mu(d\pi_+)$ is substantially different. This final quantum defect must therefore be regarded as tentative until measurements in the spectral regions between the $n=6$, $n=7$, and $n=8$ clusters can establish the position of what should be a set of strongly allowed well-separated bands with the type *c* rotational selection rules appropriate to a $^1A_2\leftarrow\tilde{C}(^1B_1)$ transition. It may be that this markedly discrepant quantum defect compensates in some way for neglect of other interactions, but there is no question that a value of $\mu(d\pi_+)$ close to the previously assumed value of 0.32[12,17,18] gives a markedly less convincing simulation.

Before examining the numerical predictions of the above quantum defect fit, it is convenient to examine the graphical simulations of the *d* and *f* series in Figs. 4–7. The program employed calculates relative intensities for transitions from a given initial orbital with well-defined *l*. Independent inten-

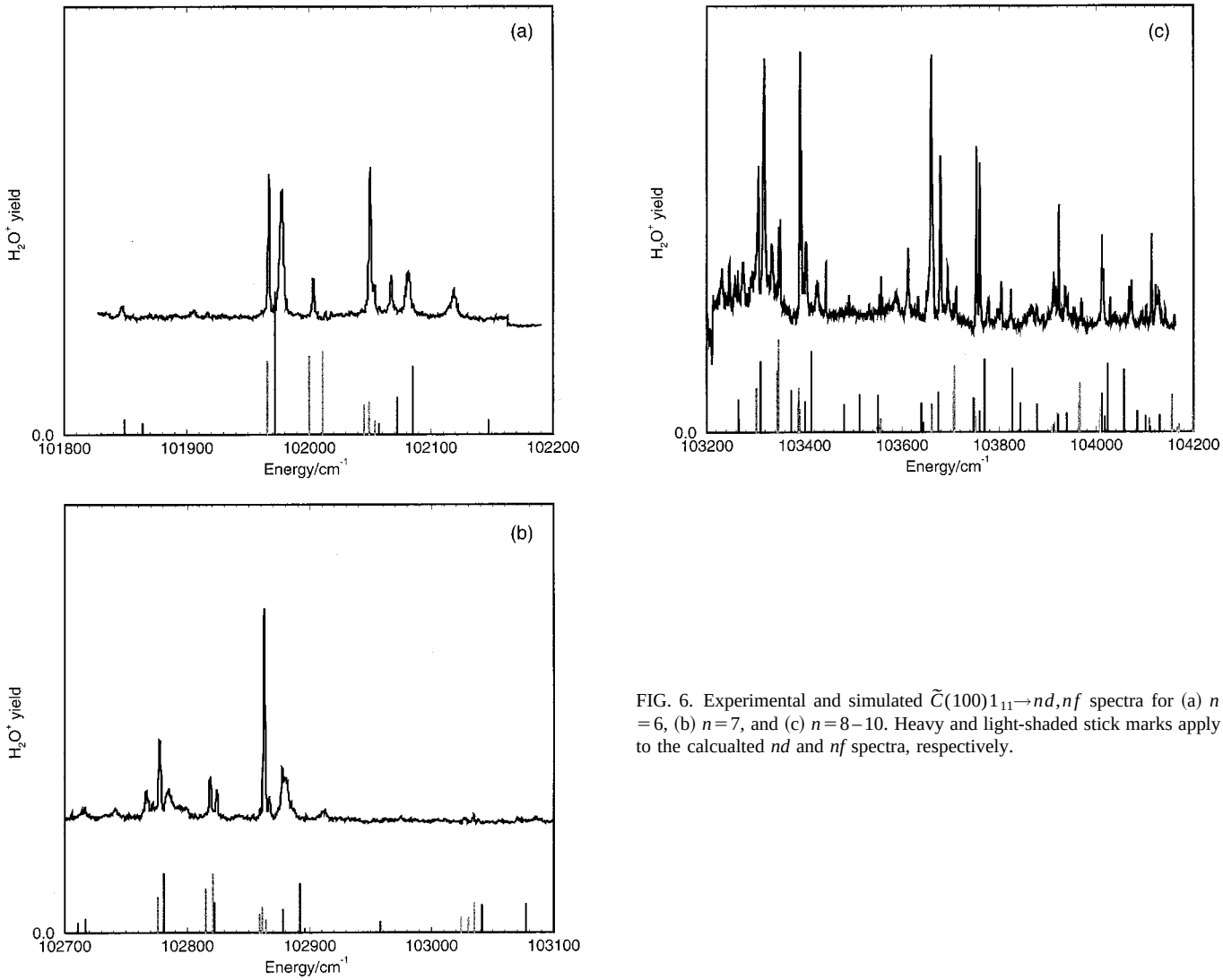

FIG. 6. Experimental and simulated $\tilde{C}(100)1_{11}\rightarrow nd,nf$ spectra for (a) $n=6$, (b) $n=7$, and (c) $n=8-10$. Heavy and light-shaded stick marks apply to the calcualted *nd* and *nf* spectra, respectively.

sity scalings have therefore been employed for the *d* and *f* series. Moreover, as discussed above, the *f* series may have intensity contributions from initial $d\sigma_+$ and $d\delta_+$ contributions to the intermediate $\tilde{C}$ state orbital; their relative intensities have been fixed in the ratio 5:1, suggested by the relative intensities of the two *f* series lines in Fig. 4(a). This relatively rough criterion is justified on the basis that absolute intensities in the photoionization spectrum of a possibly predissociating system are in any case difficult to estimate. The first observation is that the qualitative character of the fit is remarkably good, given that it is based on only $5+7$ assumed quantum defects. Not surprisingly, the *f* series simulation is generally superior to that for the *d* series, because the former lies close to Hund's case (d), with a sequence of well-developed linear series, in the sense of Fig. 1. By contrast, the much wider spread in the *d* orbital quantum defects means that the *d* series correspond to case (b) at $n=6$ but become increasingly transitional between the two cases as *n* increases. It is also evident in, for example, Fig. 5(b) that the calculation yields occasional strong calculated lines which have no experimental counterpart. The line at 102 782 cm^{-1} in Fig. 5(b) is of particular interest, because it is actually the $|7a'\rangle$ line, within the meaning of Eq. (19), whose $|6a'\rangle$ counterpart was assumed to give rise to the Coriolis coupled line pair at 101 949.9 cm^{-1} and 102 016.0 cm^{-1} in Fig. 4(a) which was used to fix the $d\pi_-$ quantum defect. The fact that the comparable lines for $n\geqslant 8$ in Fig. 4(c), which appear as $\tilde{C}\ 1_{01}\rightarrow\{110\}$ lines in Table V below, each correspond well with observed lines suggests that there is an isolated interaction at $n=7$ responsible for predissociation of this particular upper state. Such rotationally selective predissociation is well established in the lower energy spectral regions.[6,12] Finally, it is noticeable that the higher energy spectra, Figs. 4(c)–6(c), contain a significant number of unassigned lines, whose possible origins are discussed in the following section.

To complete the picture, Table VI gives a numerical comparison between observed and calculated *d* series energies. The information includes the intermediate rotational state $J''_{K''_aK''_c}$, the principal quantum number *n*, the assigned upper-state symmetry block $\{J'pp^*\}$, observed and calculated upper-state energies, and a case (b) label for states with a predominant case (b) component. The label *a* corresponds to the Coriolis mixed state $|na\rangle$ above, while *c* denotes the similar state

TABLE VI. Assignments to the *d* series. The notation $\{Jpp^*\}$ indicates the relevant upper-state symmetry block, and case (b) labels are included in the final column, where relevant. Energies are measured from the energy zero of the ground electronic state. Asterisks (*) indicate levels included in the least-squares fit.

J''	n	$\{J'pp^*\}$	E'_{obs}/cm^{-1}	E'_{calc}/cm^{-1}	Case (b)	J''	n	$\{J'pp^*\}$	E'_{obs}/cm^{-1}	E'_{calc}/cm^{-1}	Case (b)
0_{00}	6	{101}	101 879.8	101 885.2	σ_+1_{11}	*		{000}	103 403.5	103 401.3	δ_+0_{00}
*		{101}	101 993.6	101 992.3	*a*			{100}	103 426.1	(103 413.9)	δ_-1_{01}
*	7	{101}	102 804.2	102 799.2	*a*		9	{200}	103 557.5	103 551.1	π_+2_{12}
*	8	{101}	103 325.5	103 323.8	*a*			{200}	103 679.3	103 674.6	
*	9	{101}	103 685.3	103 687.1				{200}	103 753.1	103 746.8	σ_+2_{20}
*	10	{101}	103 934.4	103 932.0		*		{000}	103 760.2	103 760.3	δ_+0_{00}
*	11	{101}	104 120.7	104 122.7				{200}	103 824.2	103 827.3	
								{200}	103 876.8	103 877.3	
1_{01}	6	{110}	101 865.7	101 886.5	σ_+1_{10}	*		{000}	103 912.0	103 912.3	σ_+0_{00}
*		{110}	101 949.9	101 950.5				{200}	104 011.3	104 011.7	
*		{110}	102 012.6	102 011.1		*	10	{000}	104 014.1	104 017.2	δ_+0_{00}
		{210}	102 022.2	102 026.6	*b*			{100}	104 028.6	104 023.4	δ_-1_{01}
	7	{110}	102 721.0	102 722.2	σ_+1_{10}			{200}	104 067.3	(104 057.2)	
		{210}	102 833.4	102 833.1							
	8	{110}	103 311.8	103 315.7	*a'*	1_{10}	7	{211}	102 782.1	(102 763.7)	
		{210}	103 311.8	103 316.4				{211}	102 809.2	102 808.2	
	9	{210}	103 358.0	103 356.1	*b*			{111}	102 815.7	102 815.9	
		{110}	103 677.0	103 680.2	*a'*			{011}	102 871.0	102 873.5	δ_-0_{00}
		{010}	103 461.3	103 458.2	π_+0_{00}			{111}	102 911.0	(102 901.9)	δ_+1_{01}
		{210}	103 701.8	103 694.7							
	10	{210}	103 855.3	103 854.3	π_+2_{02}	2_{02}	6	{101}	101 879.0	101 885.2	σ_+1_{11}
		{110}	103 941.1	103 941.2	*a'*			{201}	101 981.5	101 986.4	
		{210}	103 958.3	103 964.1				{201}	102 042.0	(102 031.7)	
	11	{010}	104 016.7	104 017.5				{301}	102 073.7	102 074.9	
		{210}	104 087.2	104 086.7	π_+2_{02}			{201}	102 080.6	102 089.8	
								{301}	102 095.8	102 097.4	
1_{11*}	6	{000}	101 847.1	101 849.4	σ_+0_{00}	2_{02}	7	{101}	102 752.6	102 746.3	σ_+1_{11}
		{200}	101 977.6	101 971.5				{101}	102 801.0	102 799.2	*a*
*		{000}	102 067.1	102 071.8	δ_+0_{00}			{201}	102 813.7	102 816.9	
*		{100}	102 081.2	102 085.0	δ_-1_{01}			{201}	102 863.8	102 869.8	
						*		{301}	102 884.0	102 884.7	
1^*_{11}	7	{000}	102 716.5	102 711.3	σ_+0_{00}		8	{101}	103 322.5	103 323.8	
		{200}	102 784.8	102 781.1				{301}	103 326.9	103 329.4	
		{200}	102 824.4	102 821.9				{201}	103 354.5	103 351.6	
*		{000}	102 879.2	102 877.9	δ_+0_{00}			{301}	103 365.9	103 364.2	
		{100}	102 910.7	102 891.9	δ_-1_{01}			{201}	103 406.2	103 404.8	
								{101}	103 477.6	103 482.5	
*	8	{000}	103 264.0	103 265.8	σ_+0_{00}			{301}	103 592.7	103 593.6	
		{200}	103 317.9	103 315.7				{301}	103 748.3	103 745.1	

$$|nb\rangle = \frac{1}{\sqrt{2}}(|nd\delta_+ 2_{12}\rangle + |nd\delta_- 2_{11}\rangle, \tag{22}$$

Asterisks (*) are used to identify levels included in the least-squares fit, while entries in parentheses under E'_{calc} indicate assignments to strong calculated lines which differ by more than 10 cm^{-1} from the corresponding experimental values. The overall quality of the fit is clearly inferior to that for the *f* series in Table III, but it is remarkable that a careful fit to only five quantum defects can reproduce over 50 upper state energies to within 5 cm^{-1}, given the transitional case (b) to case (d) character of the spectrum and the possibility of relatively strong perturbations to the more penetrating *d* compared with *f* orbitals. It is also interesting to see that the case (b) character of different levels depends not only on the energy but also on the particular symmetry block $\{J'pp^*\}$ in question. For example, the case (b) and case (d) descriptions are equivalent for blocks with $J'=0$, whereas the only case (b) entries in Table V for $J'=2$ refer to the π_+ orbital, which appears to be well separated from the others. The Coriolis coupled pairs involving the near degenerate $d\delta$ orbitals, labeled *a*, *a'*, and *b*, are not of course strictly case (b), but they are labeled here as a readily identifiable recurrent feature. It is also noticeable that {100} symmetry block, accessible from $\tilde{C}\ 1_{11}$ contains a relatively unmixed δ_-1_{01} component even up to $n=10$ because levels with $K'_a=0$ cannot Coriolis couple to the close-lying $d\delta$ orbitals.

VI. CONCLUSIONS AND DISCUSSION

Multichannel quantum defect theory[12,24] has been used to analyze the double resonance photoionization spectrum of H_2O recently observed by Glab *et al.*[20,21] The most surprising feature was the presence of a strong $\tilde{C}(^1B_1)\rightarrow nf$ series, indicative of significant *d* orbital contamination of the nominal $3p(a_1)$ orbital. Definitive assignments of over 70 upper-state energy levels in the range $n=6-11$ were made, such that the resulting fit to seven *f* orbital quantum defects had a mean deviation of 2.4 cm^{-1}. Graphical extrapolation of the $\tilde{C}(100)0_{00}\rightarrow nf$ and $\tilde{C}(010)0_{00}\rightarrow nf$ series was also pre-

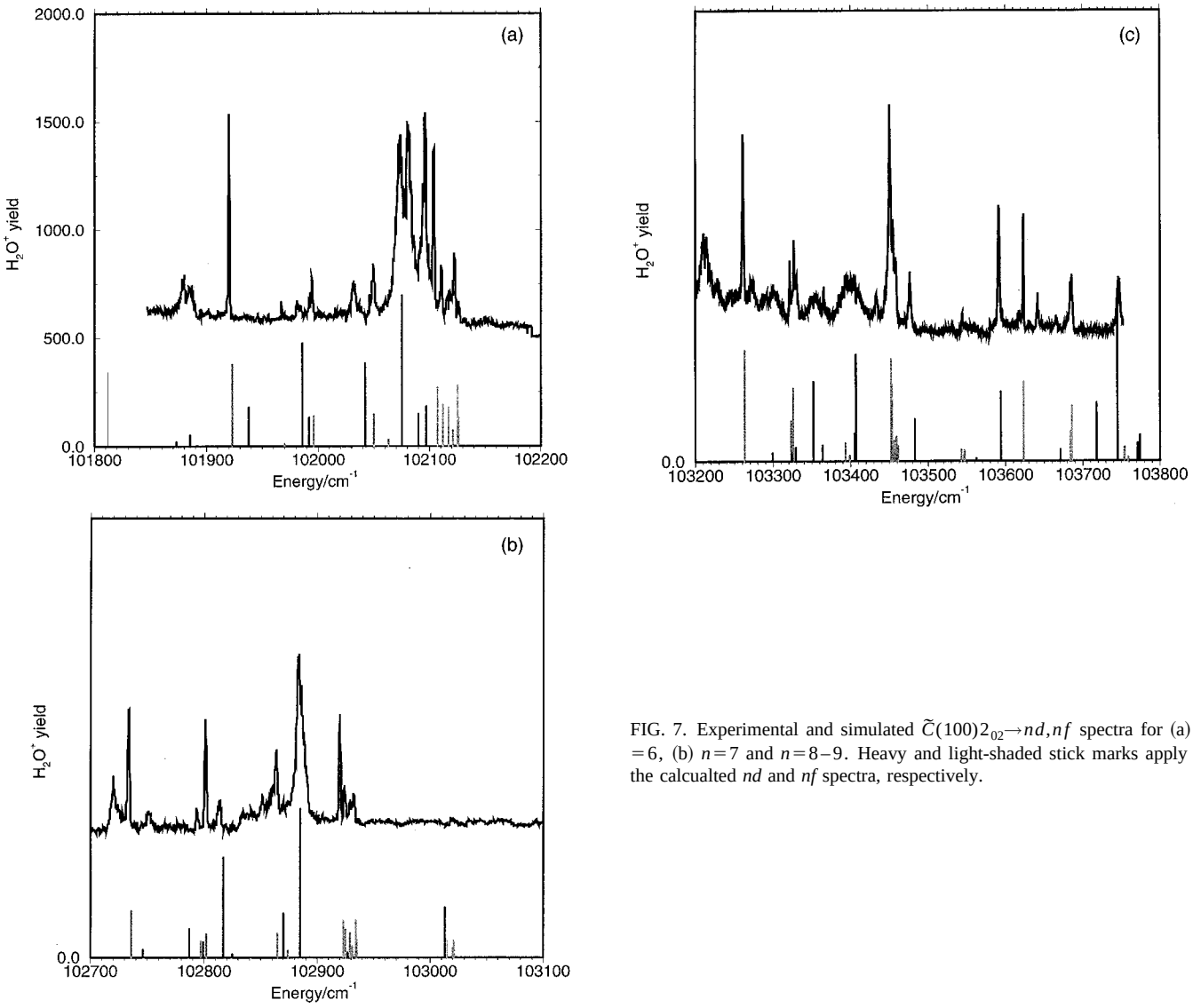

FIG. 7. Experimental and simulated $\tilde{C}(100)2_{02}\rightarrow nd,nf$ spectra for (a) $n=6$, (b) $n=7$ and $n=8-9$. Heavy and light-shaded stick marks apply to the calcualted *nd* and *nf* spectra, respectively.

sented, in the former case up to $n=27$. This is the first report of an *f* Rydberg series for any asymmetric top.

Analysis of the $\tilde{C}(^1B_1)\rightarrow nd$ series is complicated not only by the much wider spread of quantum defects, which destroys any readily discernible spectral pattern, because the various sequences of local Coriolis perturbations lead to abrupt intensity changes. It also seems likely that the greater penetrability of the *d* orbitals, compared with those with *f* character, makes them more subject to perturbations and predissociation, which are well-established features elsewhere in the spectrum.[6,7,12,13] Nevertheless, it proved possible to achieve a remarkably satisfactory simulation of the *d* series, on the assumption of only five quantum defects. Over 40 upper-state energies were reproduced within a deviation of 5 cm^{-1}, although the quantum defect for the $d\pi_+$ quantum defect, relevant to C_{2v} point group symmetry b_2, was markedly out of line with previous assumptions.[12,17,18] It should be recognized, however, that $^1A_2$ electronic symmetry of the associated states makes them optically dark to single-photon excitation from the ground state. The only firm evidence therefore comes from multiphoton detection of the $3d\widetilde{D}''(^1A_2)$ state.[3] A second consideration is that these particular $\tilde{D}''$ states appear to be well separated from the other members of each *nd* cluster, so that although they are optically accessible from $\tilde{C}(^1B_1)$, the expected well-separated bands lie outside the range of present observations, except in the relatively congested $n=8-10$ spectral regions. It would be extremely valuable to have continuous frequency scans between the presently observed $n=6$ and $n=8$ spectral regions.

The simulations of the *d* and *f* series in Figs. 4–7 show a relatively small number of unassigned lines, which are now considered. One possibility is that they arise from *s* and/or *p* series, but it is again difficult to be definitive, because the main bands are again expected to interpolate between the *nd* and *nf* clusters and hence lie outside the present observation range, except in the congested $n=8-10$ regions of Figs. 4(c), 5(c), 6(c), and 7(c). There is, however, a possible indication of local mixing between the *nd* clusters and the hitherto unobserved $np(^1A_2)$ states, because the relevant quantum defect is calculated[29] to have a value of $\mu(p\sigma_+)\approx 1.0$.

For example, even a small amount of l mixing with the distant $6d(^1A_2)$ state can lead, via Coriolis coupling, to intensity borrowing, sufficient to account for the doubled line in Fig. 4(a), if the $6p(^1A_2)$ state were close enough to the strong $6d$ feature at 101 994 cm^{-1}. A similar mechanism might lead to the strong unassigned lines at 103 950 cm^{-1} and 104 141 cm^{-1} in Fig. 4(c), but it is impossible to obtain confirmation on the basis of the present line frequencies.

[1] P. Andresen and R. Schinke, in *Molecular Photodissociation Dynamics*, edited by M. N. R. Ashfold and J. E. Baggot (Advances in Gas-Phase Photo-chemistry and Kinetics, Royal Society of Chemistry, London, 1987) Chap. 3.
[2] M. P. Docker, A. Hodgson, and J. P. Simons, in Ref. 1, Chap. 4.
[3] M. N. R. Ashfold, J. M. Bayley, and R. N. Dixon, Can. J. Phys. **62**, 1806 (1984).
[4] J. W. C. Johns, Can. J. Phys. **41**, 209 (1963).
[5] J. W. C. Johns, Can. J. Phys. **49**, 944 (1971).
[6] M. N. R. Ashfold, J. M. Bayley, and R. N. Dixon, Chem. Phys. **84**, 35 (1984).
[7] M. S. Child, Philos. Trans. R. Soc. London, Ser. A **355**, 1623 (1997).
[8] S. Bell, J. Mol. Spectrosc. **16**, 205 (1965).
[9] G. Theodorakopoulos, C. I. Nicloaides, R. J. Buenker, and S. D. Peyerimhoff, Chem. Phys. Lett. **105**, 253 (1984).
[10] D. M. Hirst and M. S. Child, Mol. Phys. **77**, 463 (1992).
[11] G. Theodorakopoulos, C. I. Nicloaides, R. J. Buenker, and S. D. Peyerimhoff, Chem. Phys. Lett. **89**, 164 (1982).
[12] R. D. Gilbert, M. S. Child, and J. W. C. Johns, Mol. Phys. **74**, 473 (1991).
[13] E. H. Abramson, J. Zhang, and D. G. Imre, J. Chem. Phys. **93**, 947 (1990).
[14] K. Watanabe and M. Zelikoff, J. Opt. Soc. Am. **43**, 753 (1953).
[15] E. Ishiguro, M. Sasanuma, H. Masuko, Y. Morioka, and M. Nakamura, J. Phys. B **11**, 993 (1978).
[16] R. H. Page, R. J. Larkin, Y. R. Shen, and Y. T. Lee, J. Chem. Phys. **88**, 2249 (1988).
[17] M. J. Vrakking, Y. T. Lee, R. D. Gilbert, and M. S. Child, J. Chem. Phys. **98**, 1902 (1993).
[18] M. S. Child and Ch. Jungen, J. Chem. Phys. **93**, 7756 (1990).
[19] O. Dutuit, A. Tabche-Fouhaile, I. Nenner, H. Frohlich, and P. M. Guyon, J. Chem. Phys. **83**, 584 (1985).
[20] W. L. Glab, J. Chem. Phys. **107**, 5979 (1997).
[21] W. L. Glab, M. S. Child, and S. T. Pratt, J. Chem. Phys. **109**, 3062 (1998).
[22] E. E. Mayer, H. G. Hedderich, and E. R. Grant, J. Chem. Phys. **108**, 1886 (1998).
[23] G. Hilber, A. Lago, and R. Wallenstein, J. Opt. Soc. Am. B **4**, 1753 (1987).
[24] C. H. Greene and Ch. Jungen, Adv. At. Mol. Phys. **21**, 51 (1985).
[25] P. R. Bunker, *Molecular Symmetry and Structure*, 2nd ed. (NRC Ottawa, 1999).
[26] R. G. Tonkyn, R. Weidmann, E. R. Grant, and M. G. White, J. Chem. Phys. **95**, 7033 (1991).
[27] J. E. Reutt, L. S. Wang, L. S. Lee, and D. A. Shirley, J. Chem. Phys. **85**, 6928 (1986).
[28] H. Lew, Can. J. Phys. **54**, 2028 (1976).
[29] G. Theodorakopoulos, I. D. Petsalakis, and M. S. Child, J. Phys. B **29**, 4543 (1996).